
Direct-Drive Implosion Experiments with Enhanced Beam Balance on OMEGA

Introduction

Laser-driven, direct-drive inertial confinement fusion (ICF) is accomplished by near-uniform illumination of spherical fuel-bearing targets with high-power laser beams.^{1–3} A goal of ICF is to achieve thermonuclear ignition and gain, which requires symmetric compression of the fuel to high temperatures (≥ 4 keV) and high areal densities (≥ 0.3 g/cm²). Both target imperfections and departures from symmetric laser illumination contribute to degradation of target performance. Low-mode ($\ell \leq 10$) perturbations of the intensity, generally due to beam-to-beam variations, can cause distortions of the core at stagnation; whereas small-scale imperfections in the target layers and in the single-beam intensity profiles contribute to higher-mode ($\ell \geq 10$) perturbations, which lead to Rayleigh–Taylor unstable growth, target breakup, and mixing of material from the shell and from the gas fill. Both can degrade target performance by reducing the peak temperature and areal density of the final fuel region.

Direct-drive ICF implosion experiments are currently being performed on LLE’s OMEGA laser system.⁴ The goal of these experiments is to attain near-ignition conditions in the compressed fuel region. Implosion experiments are being performed with both surrogate cryogenic targets^{5,6} (where the shell acts as the main fuel layer) and actual cryogenic targets⁷ (where the shell is principally solid fusion fuel). The cryogenic targets are being prepared by the newly implemented Cryogenic Target Handling System⁸ using D₂ as the fuel layer. The eventual goal is to demonstrate optimized implosions of cryogenic DT-fuel targets. Studies of the performance of surrogate fuel targets have shown that the smoothness of the individual beams has a measurable effect on target performance;^{5,6} however, the effect of beam balance on the target performance has not been quantified.⁶

This article presents a method that measures the beam-to-beam intensity variations at the target and then uses these measurements to correct the beam intensities, thereby minimizing the variations. The beam-to-beam UV intensity variations at the target are inferred from measurements of the x-ray

flux produced by each of the 60 beams of OMEGA seen separated on a 4-mm-diam, Au-coated spherical “pointing” target. Up to eight x-ray pinhole camera (XPHC) images are electronically recorded per shot from which variations in intensity are determined, taking into account view-angle effects and x-ray conversion efficiency dependence on intensity. The observed variations are then used to correct the beam intensities to produce more-uniform irradiation (or enhanced beam balance). The enhanced beam balance condition is in contrast to the standard beam balance condition arrived at by balancing the output of the laser as measured by 60 cross-calibrated full-beam calorimeters. As applied to imploding targets, the enhanced balance condition consistently yields improved symmetry of the imploding shell as observed by multiple-view x-ray imaging diagnostics. This is evidence of a more-uniform final fuel layer in the imploding target, an important goal for eventual attainment of ignition and gain.

Measurement of On-Target Intensity Using X-Ray Imaging

To accurately determine the intensity of a beam striking a laser target, it is necessary to be able to measure the full-beam intensity and/or energy before focusing and then to account for all losses incurred in transporting the beam to the target. In addition, the beam profile at its focus must be known. OMEGA uses distributed phase plates and spectrally dispersed frequency modulation to produce a time-averaged intensity pattern at the target, which is smoothed in space [smoothing by spectral dispersion (SSD)].⁹ The SSD version currently in use on OMEGA smooths the beam in two dimensions with an effective bandwidth of 1 THz and is enhanced by the use of polarization smoothing (PS).¹⁰ The smoothed beam instantaneously has a so-called super-Gaussian shape given by

$$I_{UV}(r) = I_{UV}(0) \times e^{-(r/\sigma_r)^\eta}, \quad (1)$$

where $I_{UV}(0)$ is the intensity at the beam peak, and r and σ_r are in units of distance from the beam center. Typical values for OMEGA 1-THz-SSD-with-PS beams are $\sigma_r = 300$ μm and $\eta = 2.5$.

Since the integral of Eq. (1) over time and space yields the beam energy, it is easy to see that for beams of equal size (i.e., equal σ_r and η) a measurement of the beam's peak intensity is sufficient to measure the beam energy. Here, advantage is being taken of the high UV-absorption efficiency of Au at high intensities (>90% for intensities below 10^{13} W/cm²).¹¹ Inverse-bremsstrahlung-heated Au plasmas reradiate most of their energy in the soft x-ray range (1 to 10 keV), making it possible to image the emission and, with knowledge of the x-ray conversion efficiency, to infer the UV intensity that produced the observed x-ray flux. Phenomenologically, the x-ray flux resulting from an incident intensity I_{UV} can be expressed as

$$I_x = C_{UV-x} \times I_{UV}^\gamma, \quad (2)$$

where C_{UV-x} is a constant dependent upon the x-ray band (energy range) and detection method utilized (see Subsection 3).

Spherical targets coated with Au have been used to verify beam alignment on OMEGA since target experimental operations began.¹² This method can determine the beam placement to an accuracy of $\sim 10 \mu\text{m}$. It has been noted for some time that although beam energies have been made to be nearly equal at the output of the laser, intensities on target appear to differ significantly. Figure 91.20 shows an x-ray image from a pointing target recorded by a charge-injection-device (CID), x-ray-sensitive camera¹³ at the image plane of an x-ray pinhole

camera. (The pinhole cameras use $10\text{-}\mu\text{m}$ -diam pinholes at a distance of 164 mm and a magnification of 4.0. The CID cameras have $38.5\text{-}\mu\text{m}$ -sq pixels, giving a resolution at the target of $\sim 12 \mu\text{m}$.) The pinholes themselves are covered with a $101.6\text{-}\mu\text{m}$ -thick Be foil with an additional $50.8 \mu\text{m}$ of Be between the pinhole and the detector acting as a vacuum window and a light shield for the camera. The camera sensitivity and window transmission provide for an effective energy band with a minimum of ~ 2 keV and falling sensitivity above 4 keV (see Ref. 13 for further details). Two of the beams at the center of the image have been highlighted (beams 4-2 and 4-4), and lineouts through the images are shown. Despite the fact that the beam energies are reported to be nearly equal, the peak x-ray intensities are seen to differ by a factor of ~ 2 . This suggests that either the reported energies are in error or other factors, such as beam size on target or unaccounted-for losses, differ significantly for these two beams. (These two beams were chosen since from this view the beams are at the same angle to the view direction normal; any angular effects on the observed intensity should therefore be equal.) The following method is suggested by images obtained on beam-pointing shots: Measure the beam intensities on target using a set of cross-calibrated x-ray cameras; correct the observed intensities for view-angle effects and conversion-efficiency dependence. The incident-beam-intensity variations can then be determined. Once these corrections are determined, the beam-to-beam intensity differences can then be reduced, resulting in more nearly spherical implosions. This technique and its application and results are the subject of the remainder of this article.

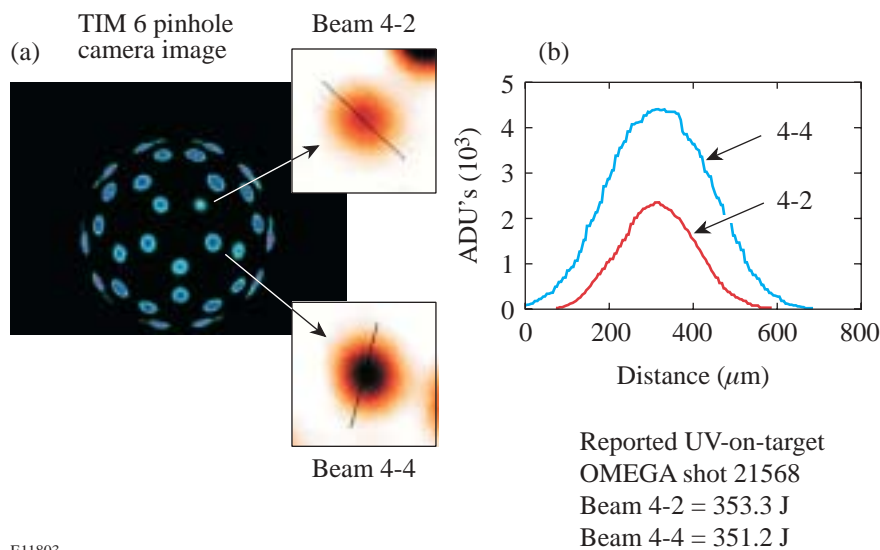


Figure 91.20

(a) TIM (ten-inch manipulator)-based pinhole camera image of a 4-mm-diam, Au-coated pointing target taken with a CID camera. Beams 4-2 and 4-4 are shown in enlarged insets. (b) Lineouts through the x-ray beam spots showing the detected intensities in analog-to-digital units (ADU's). Despite nearly equal reported energies, the peak x-ray intensities differ by about a factor of 2.

E11803

1. The View-Angle Effect on the Observed X-Ray Intensity

The effect of view angle on observed intensity has been determined by uniformly illuminating a 1-mm-diam, Au-coated sphere (Fig. 91.21) at an intensity equal to the mean intensity on a pointing shot ($\sim 10^{14}$ W/cm²). Since all beams now overlap, the individual beam energies are ~ 6 times lower. The azimuthally averaged radial lineout of the x-ray image [Fig. 91.21(b)] is seen to closely match that expected from an optically thin plasma shell, as characterized by

$$I_x(r) = I_x(0) \times (r_0/\Delta r) \times \left[\sqrt{(1 + \Delta r/r_0)^2 - (r/r_0)^2} - \sqrt{1 - (r/r_0)^2} \right], \quad (3)$$

where $I_x(0)$ is the intensity observed at the center of the image (face-on), r is the distance in the target plane from the center of the image, r_0 is the plasma emission radius, and Δr is the plasma thickness. The profile of Fig. 91.21(b) is best fit by values of $r_0 = 500 \mu\text{m}$ and $\Delta r = 113 \mu\text{m}$.

2. Camera Cross-Calibration

Up to eight x-ray cameras are used on a pointing shot, producing different views of the beams on target. To compare beam images from two cameras, the view-angle effect must be removed, leaving only the difference in collection solid angle (pinhole area) and camera gain. Figure 91.22 shows one such comparison of beam peak intensities seen from two cameras after correcting for the view-angle effect using Eq. (3) and using the best-fit parameters as determined from the results shown in Fig. 91.21 ($\Delta r = 113 \mu\text{m}$, whereas $r_0 = 2 \text{ mm}$ for these

targets). The observed intensities follow a straight line with a zero intercept and a slope equal to the ratio of the sensitivity of the two cameras.

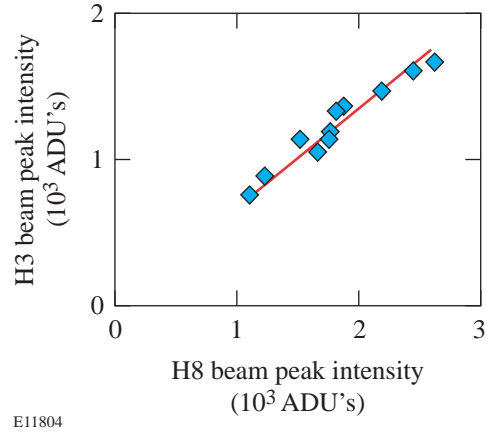


Figure 91.22

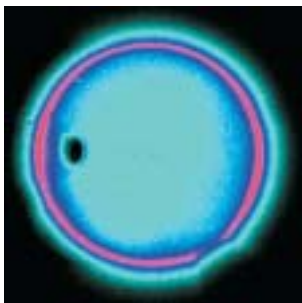
View-angle-corrected beam peak intensities as viewed by two x-ray pinhole cameras. The straight-line correlation demonstrates the validity of the view-angle correction and determines the cross-calibration factor for the two cameras.

3. Conversion-Efficiency Dependence and Determination of On-Target Beam-to-Beam Variation

An estimate of the power-law conversion of UV to x rays was determined by varying a single-beam energy, yielding a value of γ in Eq. (2) of ~ 3.7 . This preliminary value was then used when fitting values of the observed beam shapes. Combining Eqs. (1) and (2) yields

$$I_x(r) = I_x(0) \times \left[e^{-(r/\sigma_r)^\eta} \right]^\gamma, \quad (4)$$

(a) CID image (H6 view)



E11296

(b) Radial profile

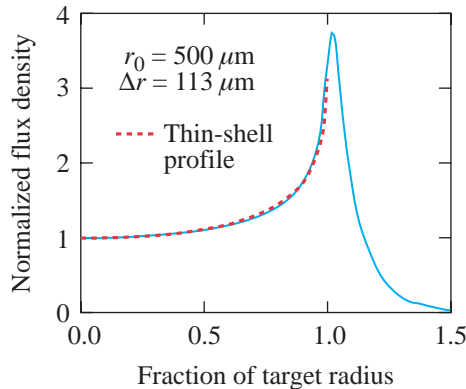


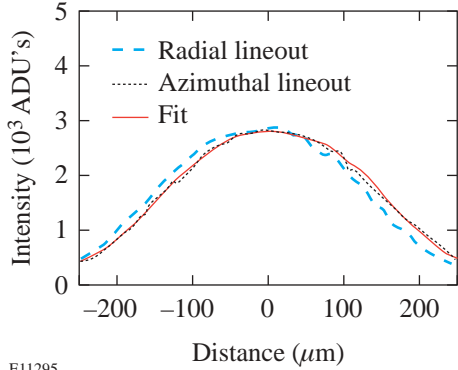
Figure 91.21

(a) An x-ray pinhole camera image of a uniformly illuminated, 1-mm-diam, Au-coated sphere used to determine the angular effect on the observed surface flux density. (b) The azimuthally averaged radial profile of the uniformity target. Regions of the target not covered by gold (at points of support during coating) were excluded from the azimuthal averaging.

where

$$I_x(0) = C_{UV-x} \times [I_{UV}(0)]^\gamma \tag{5}$$

Figure 91.23 shows a fit of a single beam (4-4) to Eq. (4). The peak values are determined in this manner for every beam by using up to eight pinhole cameras.



E11295

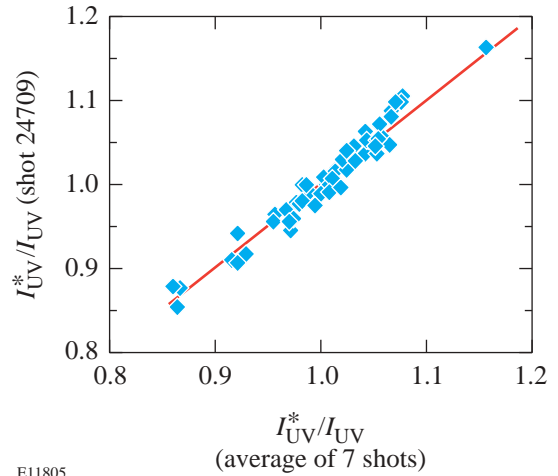
Figure 91.23
Fit to a single-beam x-ray intensity profile using a super-Gaussian with power-law x-ray conversion efficiency [Eq. (4)].

With a set of cross-calibrated cameras, variations from beam to beam can be determined for all 60 beams of OMEGA. During laser system operation, some beam-energy variation occurs due to variations in amplification and input beam (driver line) energy. System calorimeters [e.g., high-energy diodes (HED’s)] are used to account for these variations. If beam-energy variations are accounted for by variations in the HED-measured beam energies, then beam-to-beam variations not due to beam-energy variations should remain the same and show up as differences on target. This is seen in a plot of the ratio of the normalized inferred peak UV intensity I_{UV}^* derived from x-ray imaging to the normalized HED determined UV intensity I_{UV} for all 60 beams on one shot as compared with the average of the same for seven shots (Fig. 91.24). The values are seen to be stable despite large variations in beam energy. Using the average values of these ratios, R_i is given by

$$R_i = I_{UV_i}^* / E_{UV_i}^* \tag{6}$$

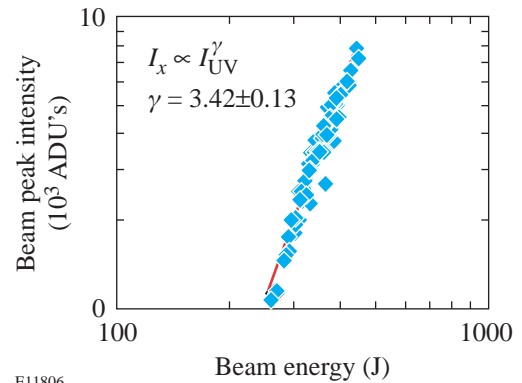
where $I_{UV_i}^*$ is the normalized x-ray-inferred UV peak intensity and $E_{UV_i}^*$ is the HED-determined normalized UV energy on

target (both for the i th beam). Applying these corrections to the HED-measured energies allows for a more accurate determination of the power-law conversion parameter γ [Eq. (4)]. A best-fit value of $\gamma = 3.42 \pm 0.13$ is seen to fit the observed x-ray to UV variation (Fig. 91.25).



E11805

Figure 91.24
Values of the ratios of the normalized x-ray-inferred beam peak intensities to the normalized HED-inferred beam energies for all 60 beams determined from one pointing shot versus the same values averaged over seven shots. Each data point represents a different beam. The beam energies were purposely varied from ~250 to 440 J, resulting in little change in these ratios despite nearly 100% changes in the peak x-ray intensity.



E11806

Figure 91.25
The observed peak x-ray intensities corrected for view-angle effect as a function of the corrected beam energies. The dependence follows a power law of $\gamma = 3.42 \pm 0.13$.

Enhanced On-Target Beam Balance

In the standard balance technique, the gains in the amplifiers by stage, and the losses by stage (primarily in the split regions), are adjusted to produce equal beam energies at the system output calorimeters. The UV energies on target are inferred from continuous-wave (cw) laser measurements of the losses incurred in each beam by the mirrors, lenses, diffracting optics, vacuum windows, and debris shields from the system output calorimeters to the target (i.e., from the transport to the target). Variations of these losses are kept to a minimum by replacement of the poorest-performing elements. In contrast, the enhanced balance technique uses the measured x-ray intensities at the target to determine the gain of the last IR amplifier required to produce equal intensities (x-ray and, hence, by inference UV also) at the target. An algorithm has been developed by which a beam's desired UV energy output can be achieved with a variation in the capacitor-bank voltage of the final disk amplifier.

Using the measured values of R_i , it is possible to further minimize on-target variations by iteration. From Eq. (6) it follows that

$$I_{UVi}^* = R_i \times E_{UVi}^* \quad (7)$$

The normalized beam energies are varied to attempt to make all values of I_{UVi}^* equal to 1. The adjustments are made by changing the capacitor bank voltage of the last amplifier and by observing the resultant change in output energy. The response follows the equation

$$E_{UV} = E_{IR} \times G_{amp}(V_{bank}) \times \epsilon_{UV}, \quad (8)$$

where E_{UV} is the inferred UV energy, E_{IR} is the input IR energy, G_{amp} is the gain of the laser amplifier for a capacitor bank voltage of V_{bank} , and ϵ_{UV} is the efficiency of the UV conversion crystals, which is also a function of G_{amp} and E_{IR} .

Figure 91.26 shows a comparison of a standard balance pointing shot (in which IR variations are minimized) to an enhanced balance pointing shot (in which peak-intensity variations are minimized). The standard balance shot [Fig. 91.26(a)] has a small variation in the HED-determined energies [$\sigma_{rms}(E_{UV}) = 2.8\%$], but a large variation in the inferred normalized UV beam peak intensities [$\sigma_{rms}(I_{UV}^*) = 6.6\%$]. Conversely, the enhanced balance shot [Fig. 91.26(b)] has a larger HED-determined variation [$\sigma_{rms}(E_{UV}) = 6.0\%$], but a

smaller variation in the inferred normalized UV beam peak intensities [$\sigma_{rms}(I_{UV}^*) = 2.2\%$]. The beam-to-beam variations have been reduced by about a factor of 3.

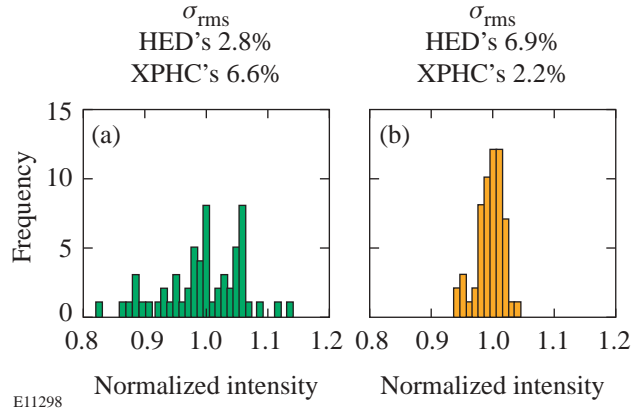


Figure 91.26

The inferred UV beam peak intensity distribution for all 60 beams of OMEGA determined on (a) a standard balance pointing shot and (b) an enhanced balance pointing shot.

Enhanced-Balance Implosion Experiments

With the enhanced-balance-correction constants R_i determined, the beam peak intensities can be inferred from the HED-determined beam energies corrected by the enhanced-correction constants R_i . Figure 91.27 shows x-ray microscope images of a set of implosions performed with standard balance and enhanced balance. Three pairs of targets were used. All were 930- μm -diam, 18.5- μm -thick CH shells filled with 15, 7, and 3 atm of D_2 gas, respectively. A clear difference is seen in the shape of the core apparently due to the change in direct-drive illumination uniformity. [The two cases had average values of $\sigma_{rms}(I_{UV}^*) = 6.0\%$ for the standard balance condition and 2.2% for the enhanced balance condition.] Figure 91.28 shows another comparison of core shape for a different shell thickness (27 μm) and fill pressure (20 atm D_2). All enhanced balance implosions show more-symmetric cores; however, small-scale structure is common to both cases.

Analysis of the angular dependence of the illumination uniformity demonstrates the effect on the implosion. The calculated overlap intensity shown in Fig. 91.29 is displayed in an Aitoff projection for the standard-balance, 15-atm-filled case (shot 24119, see Fig. 91.27). The overlap intensity calculation assumes HED-measured beam energies corrected for by

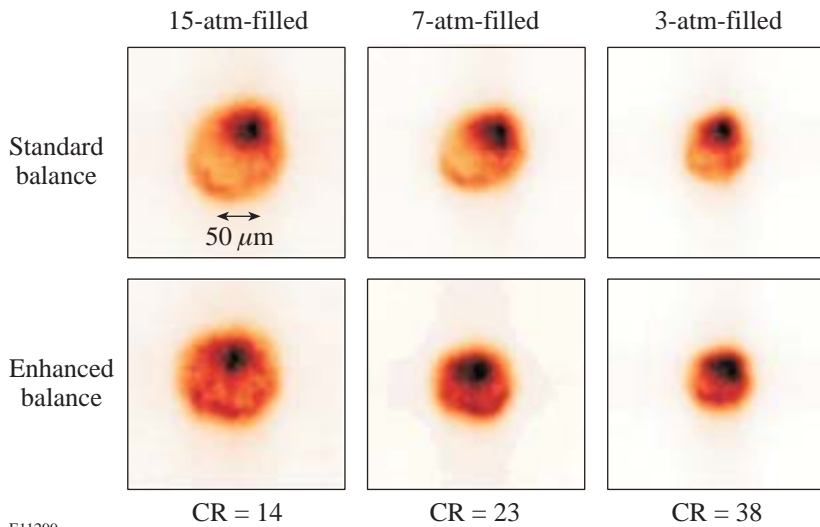
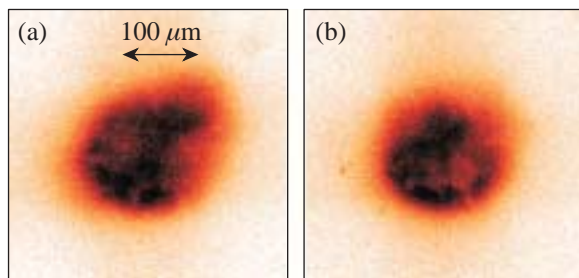


Figure 91.27 Direct-drive implosion experiments performed on OMEGA with 18.5- μm -thick CH shells filled with 15, 7, and 3 atm of D_2 gas. All shots were with ~ 23 kJ of UV on target in a 1-ns square pulse, using 1-THz SSD with PS. The enhanced balance implosions show a more-uniform spherical stagnation region. The calculated convergence ratios for these implosions (initial fuel-shell interface radius divided by final radius, CR) are indicated.

E11299

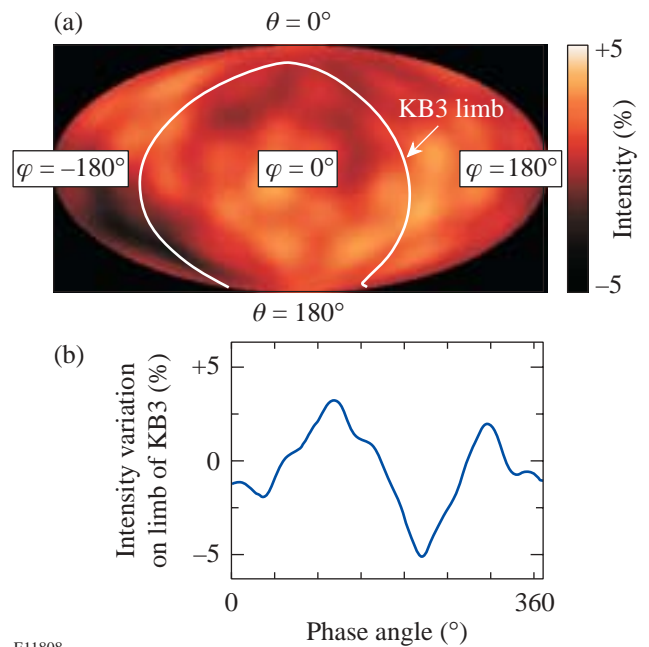
the enhanced balance analysis [Eq. (7)] with all beams having the same super-Gaussian profile ($r_0 = 300 \mu\text{m}$ and $\eta = 2.5$). Absorption is modeled by a simple cosine dependence on the angle the rays make with the target normal. The individual peaks seen are at the overlap of five or six beams and are due to the imperfect overlap of the OMEGA beams with the given target size, number of beams, and beam shape ($\sim 1.5\%$ peak to valley for perfect beam balance). Also shown is a lineout through the computed intensity pattern as would impinge on the limb of the target as seen from the x-ray microscope. The intensity pattern has an $\sim 7\%$ peak-to-valley variation with two minima at 40° and 220° and maxima at 120° and 290° , where

the angle referred to is clockwise with respect to the vertical. After applying enhanced balance, the intensity variations due to beam balance are reduced to less than 2%.



E11807

Figure 91.28 Comparison of KB (Kirkpatrick-Baez) microscope-imaged implosion cores for a pair of 27- μm -thick CH shells filled with 20 atm of D_2 , (a) with standard balance and (b) with enhanced balance. The enhanced balance implosion again shows a more spherically shaped core.



E11808

Figure 91.29 (a) The calculated overlap intensity on a standard balance implosion (OMEGA shot 24119) presented as an Aitoff projection of the entire spherical surface. The measurements from the pointing shots infer a peak to valley of 7%. (b) The lineout through the limb of the target as seen from the KB microscope used in Figs. 91.27 and 91.28.

An *ORCHID*¹⁴ 2-D hydrocode simulation was performed using the calculated intensity on the target limb from phase angle 40° to 220° for the axisymmetric laser illumination. Radiation transport is not included in this simulation. The effect of radiation losses, however, was accounted for by lowering the effective incident intensity. By its nature, a 2-D simulation can only simulate axisymmetric flow. Figure 91.30 shows the result of the simulation near the time of maximum shell compression showing a slightly distorted core with an ellipticity $e = 1.08$. Shown as an inset is the observed x-ray image with the axis of the minima in the calculated intensity indicated. The ellipticity of the core image and the simulation are in good agreement, confirming that the main effect is explained by a measurable beam imbalance. Correcting the beam imbalance nearly removes the residual ellipticity as a result of the more-uniform illumination by the 60 beams of OMEGA.

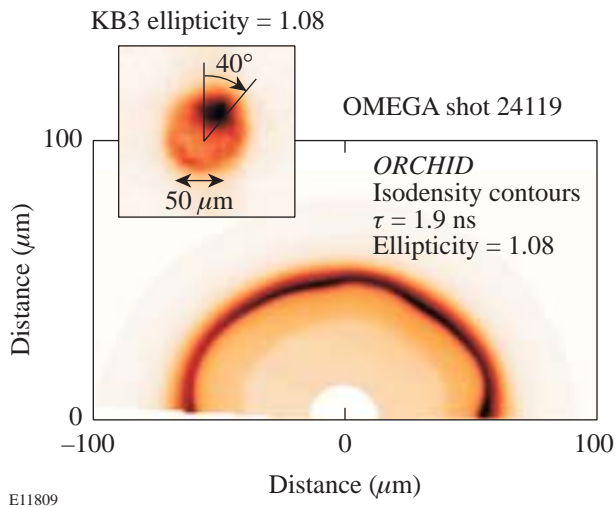


Figure 91.30
Isodensity contours from an *ORCHID* 2-D hydrocode simulation of the implosion of an 18.5- μm -thick, 15-atm-filled CH shell (OMEGA shot 24119). The time of this snapshot is 1.9 ns from the start of the laser pulse (near the time of maximum shell compression). The input intensities used were those calculated for this experiment and occurring on the limb of the target as observed from the KB microscope. The corresponding image is shown as an inset with the symmetry axis of the 2-D simulation indicated.

The symmetry of the implosions appears to correlate with the beam balance. To determine the effects on other measures of target performance, a series of implosion experiments were performed with 1-THz SSD smoothing with PS and 1-ns square pulses. The targets ranged from 18 to 25 μm in thickness

and were filled with 3 or 15 atm of D_2 gas. Figure 91.31(a) shows the ratio of the measured D-D neutron yield to the *LILAC* hydrocode¹⁵-predicted yield [yield over calculated (YOC)] for these experiments. This measure of target performance is used as a means of comparison to account for differences in energy on target and shell-thickness differences from shot to shot. The enhanced balance target implosions were performed with slightly less energy (typically 21 kJ on enhanced balance shots and 23 kJ on standard balance shots) since after correction for imbalance, some beams could not be raised to sufficiently high levels, necessitating all others to be lowered. The results are seen to follow the included trend lines (dashed) with little obvious difference due to balance condition. Figure 91.31(b) shows the measured ratio of D-T neutron secondary yield to D-D neutron primary yield in these same experiments. [The only difference between the two balance conditions is the apparent larger variation in the standard balance values of the 15-atm-filled target implosions. Despite a definite change to more-symmetric shell stagnations, the primary and secondary neutron yield measurements indicate little dependence of target performance on balance condition (at least

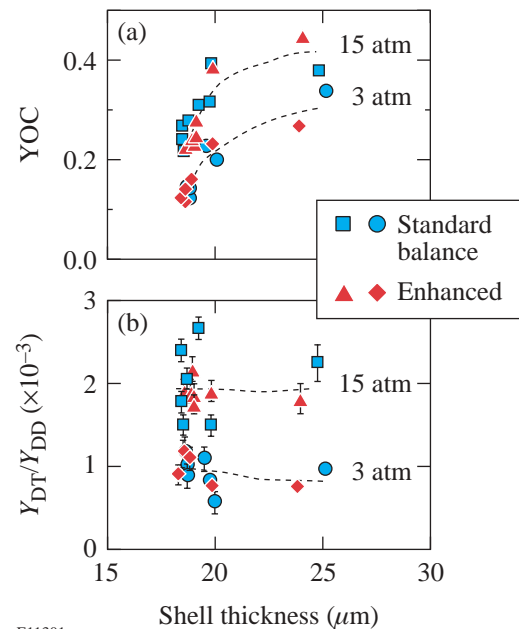


Figure 91.31
Measurements of the fusion yield's dependence on balance condition from a set of 3- and 15-atm- D_2 -filled CH shell implosions: (a) the ratio of the measured to the simulated primary D-D neutron yield; (b) the ratio of the measured secondary DT neutron yield to the measured primary D-D neutron yield.

with these measurements).] Whereas, it has been shown in past experiments that these measurements show a dependence on single-beam smoothing.^{5,6,10}

Additional measurements of the directional dependence of the total ρR at the time of peak fusion production have recently been reported by Séguin *et al.*¹⁶ Their measurements are derived from the slowing down of 14.7-MeV D-He³ fusion reaction-generated protons observed from different directions around the target. They find that the observed ρR asymmetries are significantly different for the two balance conditions reported in this work (standard and enhanced). Although asymmetries still exist, they appear to be lower when the optimum x-ray-inferred enhanced balance condition is imposed.

Conclusions

A method for determining and optimizing the beam-to-beam intensity variation of the 60 beams of the OMEGA laser system, as configured for direct-drive illumination (with 1-THz SSD and polarization smoothing), has been developed. This method infers the beam-to-beam energy balance by direct observation of x rays emitted by Au plasmas produced by OMEGA's focused high-power laser beams. The UV energy balance is determined from the observed x-ray balance by taking into account x-ray conversion efficiency and view-angle effects in a semi-empirical manner. Optimized or enhanced balance is achieved by removing the precisely determined beam-to-beam energy variation by adjusting the gain of the last amplifier. The method has achieved a three-fold reduction in the beam imbalance, from an inferred level of ~6% (rms) to ~2% (rms).

Direct-drive implosions with enhanced beam balance consistently show more spherically shaped stagnation cores. A 2-D hydrocode simulation of an uncorrected (standard balance) implosion shows that the magnitude and direction of the resulting core distortion are consistent with arising from beam imbalance. In contrast there is little effect on the YOC ratio or fuel areal density.

The small differences in beam-to-beam energy (<10%) have not been explained by repeated measurements of transport losses in the mirrors, lenses, diffracting optics, and windows. It is likely that the differences are due to scattering losses not accounted for by the spatially integrating techniques employed to measure transport and can be determined only by a technique, such as described in this work, that measures the intensity at the target with calibrated imaging diagnostics.

ACKNOWLEDGMENT

This work was supported by the U.S. Department of Energy Office of Inertial Confinement Fusion under Cooperative Agreement No. DE-FC03-92SF19460 and the University of Rochester. The support of DOE does not constitute an endorsement by DOE of the views expressed in this article.

REFERENCES

1. J. Nuckolls *et al.*, *Nature* **239**, 139 (1972).
2. J. D. Lindl, *Inertial Confinement Fusion: The Quest for Ignition and Energy Gain Using Indirect Drive* (Springer-Verlag, New York, 1998), Chap. 6, pp. 61–82.
3. S. E. Bodner, D. G. Colombant, J. H. Gardner, R. H. Lehmberg, S. P. Obenshain, L. Phillips, A. J. Schmitt, J. D. Sethian, R. L. McCrory, W. Seka, C. P. Verdon, J. P. Knauer, B. B. Afeyan, and H. T. Powell, *Phys. Plasmas* **5**, 1901 (1998).
4. T. R. Boehly, D. L. Brown, R. S. Craxton, R. L. Keck, J. P. Knauer, J. H. Kelly, T. J. Kessler, S. A. Kumpan, S. J. Loucks, S. A. Letzring, F. J. Marshall, R. L. McCrory, S. F. B. Morse, W. Seka, J. M. Soures, and C. P. Verdon, *Opt. Commun.* **133**, 495 (1997).
5. F. J. Marshall, J. A. Delettrez, V. Yu. Glebov, R. P. J. Town, B. Yaakobi, R. L. Kremens, and M. Cable, *Phys. Plasmas* **7**, 1006 (2000).
6. F. J. Marshall, J. A. Delettrez, R. Epstein, V. Yu. Glebov, D. R. Harding, P. W. McKenty, D. D. Meyerhofer, P. B. Radha, W. Seka, S. Skupsky, V. A. Smalyuk, J. M. Soures, C. Stoeckl, R. P. Town, B. Yaakobi, C. K. Li, F. H. Séguin, D. G. Hicks, and R. D. Petrasso, *Phys. Plasmas* **7**, 2108 (2000).
7. C. Stoeckl, C. Chiritescu, J. A. Delettrez, R. Epstein, V. Yu. Glebov, D. R. Harding, R. L. Keck, S. J. Loucks, L. D. Lund, R. L. McCrory, P. W. McKenty, F. J. Marshall, D. D. Meyerhofer, S. F. B. Morse, S. P. Regan, P. B. Radha, S. Roberts, T. C. Sangster, W. Seka, S. Skupsky, V. A. Smalyuk, C. Sorce, J. M. Soures, R. P. J. Town, J. A. Frenje, C. K. Li, R. D. Petrasso, F. H. Séguin, K. Fletcher, S. Padalino, C. Freeman, N. Izumi, R. Lerche, and T. W. Phillips, *Phys. Plasmas* **9**, 2195 (2002).
8. Laboratory for Laser Energetics LLE Review **81**, 6, NTIS document No. DOE/SF/19460-335 (1999). Copies may be obtained from the National Technical Information Service, Springfield, VA 22161.
9. S. Skupsky, R. W. Short, T. Kessler, R. S. Craxton, S. Letzring, and J. M. Soures, *J. Appl. Phys.* **66**, 3456 (1989).
10. D. D. Meyerhofer, J. A. Delettrez, R. Epstein, V. Yu. Glebov, V. N. Goncharov, R. L. Keck, R. L. McCrory, P. W. McKenty, F. J. Marshall, P. B. Radha, S. P. Regan, S. Roberts, W. Seka, S. Skupsky, V. A. Smalyuk, C. Sorce, C. Stoeckl, J. M. Soures, R. P. J. Town, B. Yaakobi, J. D. Zuegel, J. Frenje, C. K. Li, R. D. Petrasso, D. G. Hicks, F. H. Séguin, K. Fletcher, S. Padalino, M. R. Freeman, N. Izumi, R. Lerche, T. W. Phillips, and T. C. Sangster, *Phys. Plasmas* **8**, 2251 (2001).
11. P. D. Goldstone, J. A. Cobble, A. Hauer, G. Stradling, W. C. Mead, S. R. Goldman, S. Coggeshall, M. C. Richardson, P. A. Jaanimagi, O. Barnouin, R. Marjoribanks, B. Yaakobi, F. J. Marshall, P. Audebert, and J. Knauer, in *X Rays from Laser Plasmas*, edited by M. C. Richardson (SPIE, Bellingham, WA, 1987), Vol. 831, pp. 54–61.

12. J. M. Soures, R. L. McCrory, C. P. Verdon, A. Babushkin, R. E. Bahr, T. R. Boehly, R. Boni, D. K. Bradley, D. L. Brown, R. S. Craxton, J. A. Delettrez, W. R. Donaldson, R. Epstein, P. A. Jaanimagi, S. D. Jacobs, K. Kearney, R. L. Keck, J. H. Kelly, T. J. Kessler, R. L. Kremens, J. P. Knauer, S. A. Kumpan, S. A. Letzring, D. J. Lonobile, S. J. Loucks, L. D. Lund, F. J. Marshall, P. W. McKenty, D. D. Meyerhofer, S. F. B. Morse, A. Okishev, S. Papernov, G. Pien, W. Seka, R. Short, M. J. Shoup III, M. Skeldon, S. Skupsky, A. W. Schmid, D. J. Smith, S. Swales, M. Wittman, and B. Yaakobi, *Phys. Plasmas* **3**, 2108 (1996).
13. F. J. Marshall, T. Ohki, D. McInnis, Z. Ninkov, and J. Carbone, *Rev. Sci. Instrum.* **72**, 713 (2001).
14. R. L. McCrory and C. P. Verdon, in *Inertial Confinement Fusion*, edited by A. Caruso and E. Sindoni (Editrice Compositori, Bologna, Italy, 1989), pp. 83–124.
15. M. C. Richardson, P. W. McKenty, F. J. Marshall, C. P. Verdon, J. M. Soures, R. L. McCrory, O. Barnouin, R. S. Craxton, J. Delettrez, R. L. Hutchison, P. A. Jaanimagi, R. Keck, T. Kessler, H. Kim, S. A. Letzring, D. M. Roback, W. Seka, S. Skupsky, B. Yaakobi, S. M. Lane, and S. Prussin, in *Laser Interaction and Related Plasma Phenomena*, edited by H. Hora and G. H. Miley (Plenum Publishing, New York, 1986), Vol. 7, pp. 421–448.
16. F. H. Séguin, C. K. Li, J. A. Frenje, S. Kurebayashi, R. D. Petrasso, F. J. Marshall, D. D. Meyerhofer, J. M. Soures, T. C. Sangster, C. Stoeckl, J. A. Delettrez, P. B. Radha, V. A. Smalyuk, and S. Roberts, *Phys. Plasmas* **9**, 3558 (2002).